AGU PUBLICATIONS

JGR

Journal of Geophysical Research: Atmospheres

RESEARCH ARTICLE

10.1002/2016JD026404

Key Points:

- To compensate for the smaller net cooling effect, warm clouds in PNNL-MMF are optically thicker and warmer than the observations
- The biases in simulated clouds result from a combination of microphysical and dynamical errors rather than subgrid scale errors
- The PNNL-MMF produces about the correct mean rain rate to satisfy atmospheric energy balance with an incorrect distribution of rates

Correspondence to:
H. Takahashi,
hanii.takahashi@jpl.nasa.gov

Citation:
Takahashi, H., M. Lebsock, K. Suzuki, G. Stephens, and M. Wang (2017), An investigation of microphysics and subgrid-scale variability in warm-rain clouds using the A-Train observations and a multiscale modeling framework, *J. Geophys. Res. Atmos.*, *122*, 7493–7504, doi:10.1002/2016JD026404.

Received 20 DEC 2016
Accepted 25 JUN 2017
Accepted article online 28 JUN 2017
Published online 24 JUL 2017

An investigation of microphysics and subgrid-scale variability in warm-rain clouds using the A-Train observations and a multiscale modeling framework

Hanii Takahashi[1,2], Matthew Lebsock[2], Kentaroh Suzuki[3], Graeme Stephens[2,4], and Minghuai Wang[5,6]

[1]Joint Institute for Regional Earth System Science and Engineering, University of California, Los Angeles, California, USA, [2]Jet Propulsion Laboratory, California Institute of Technology, Pasadena, California, USA, [3]Atmosphere and Ocean Research Institute, University of Tokyo, Chiba, Japan, [4]Department of Meteorology, University of Reading, Reading, UK, [5]Institute for Climate and Global Change Research, and School of Atmospheric Sciences, Nanjing University, Nanjing, China, [6]Collaborative Innovation Center of Climate Change, Nanjing, China

Abstract A common problem in climate models is that they are likely to produce rain at a faster rate than is observed and therefore produce too much light rain (e.g., drizzle). Interestingly, the Pacific Northwest National Laboratory (PNNL) multiscale modeling framework (MMF), whose warm-rain formation process is more realistic than other global models, has the opposite problem: the rain formation process in PNNL-MMF is less efficient than the real world. To better understand the microphysical processes in warm cloud, this study documents the model biases in PNNL-MMF and evaluates warm cloud properties, subgrid variability, and microphysics, using A-Train satellite observations to identify sources of model biases in PNNL-MMF. Like other models PNNL-MMF underpredicts the warm cloud fraction with compensating large optical depths. Associated with these compensating errors in cloudiness are compensating errors in the precipitation process. For a given liquid water path, clouds in the PNNL-MMF are less likely to produce rain than are real-world clouds. However, when the model does produce rain it is able to produce stronger precipitation than reality. As a result PNNL-MMF produces about the correct mean rain rate with an incorrect distribution of rates. The subgrid variability in PNNL-MMF is also tested, and results are fairly consistent with observations, suggesting that the possible sources of model biases are likely to be due to errors in its microphysics or dynamics rather than errors in the subgrid-scale variability produced by the embedded cloud resolving model.

1. Introduction

Microphysical processes in warm clouds play a significant role in controlling the energy budget and hydrological cycle, and thus, these processes are of fundamental importance to the global climate. However, they are generally not well represented by models. A fundamental challenge in modeling is to parameterize important processes that cannot be resolved at grid scale in climate models [*Prein et al.*, 2015], which can be a major source for model errors and uncertainties in future climate projections [e.g., *Ellingson et al.*, 1991; *Henderson-Sellers et al.*, 1993; *Pedersen and Winther*, 2005; *Déqué et al.*, 2007].

A previous study using one particular model demonstrated that the global surface temperature trends in present-day simulations largely depend on the threshold particle radius for warm rain to occur and pointed out that the model whose threshold particle radius (~6.0 μm) is smaller than the reality (~10.0 μm) can reproduce the most realistic temperature trend [*Golaz et al.*, 2013; *Suzuki et al.*, 2013]. To prioritize producing realistic global mean climate projections over realistic microphysical processes by using smaller threshold particle radius likely to produce rain at a faster rate than is observed, and therefore produce too much light rain such as drizzle, which is a common problem in some models [*Stephens et al.*, 2010]. Overproduction of drizzle can cause additional problems in lifetime duration and evolution of clouds [*Miller et al.*, 1998; *Albrecht*, 1989; *Albrecht*, 1993; *Wood*, 2000], and thus, understanding how the microphysical process in warm clouds takes place in real clouds is of great importance.

Subgrid variability also plays an important role in the microphysical process [*Pincus and Klein*, 2000; *Huang and Liu*, 2014; *Raut and Larson*, 2016]. It has been known that neglecting subgrid variability of clouds and

instead computing grid mean microphysical process rates directly from grid-average cloud properties can cause large biases in the calculated microphysical process rates. Therefore, climate models generally need to integrate subgrid variability over a grid box to simulate grid-box averaged rates of microphysical processes. In order to improve model performance, it is important to understand and physically represent the subgrid variability in models.

The coalescence process in models can be approximated as the combination of two processes: autoconversion and accretion. While autoconversion directly turns cloud water to rainwater, accretion collects cloud water by falling rain. Precipitation formation is mainly triggered by the autoconversion process where coagulations among cloud particles play a key role. A previous study by *Suzuki et al.* [2015], hereafter S15, examined the simulated microphysical process over the global ocean with different autoconversion schemes. They demonstrated that the Pacific Northwest National Laboratory (PNNL) multiscale modeling framework (MMF) [*Wang et al.*, 2011a, 2011b], whose autoconversion process is based on *Khairoutdinov and Kogan* [2000], simulates the most realistic warm-rain formation process of all analyzed models.

PNNL-MMF is an extension of a MMF that has an embedded 2-D cloud-resolving model (CRM) in place of parameterizations in each grid column of a general circulation model (GCM). Unlike other models in S15 whose rain schemes are diagnostic, PNNL-MMF has a prognostic rain scheme. S15 demonstrated that models that have prognostic schemes represented better warm-rain formation process compared to the models that have diagnostic schemes. Also, PNNL-MMF can clearly predict cloud and precipitation profiles at a cloud resolving horizontal resolution. Therefore, it is not surprising that PNNL-MMF represents the most realistic warm-rain formation process compared to other global models analyzed in S15, which use simpler schemes to parameterize moist processes.

Although PNNL-MMF has a more realistic warm-rain formation process than other global models, S15 reveals that the rain formation in PNNL-MMF is less efficient than the real world and other models. This is interesting because generally models' rain efficiencies are too high [*Stephens et al.*, 2010], and the problems in PNNL-MMF are different from other models. Therefore, we focus on PNN-MMF in this study. It is worth diagnosing the possible sources of model biases in PNNL-MMF such as microphysical parameterization or subgrid variability to better understand and improve simulated warm-rain clouds.

The present paper demonstrates and documents the utility for using the A-Train observations to evaluate model biases. To better understand the microphysical process in warm cloud, we evaluate cloud properties, subgrid variability, and microphysics in PNNL-MMF using A-Train satellite observations [*Stephens et al.*, 2002] to identify the major sources of model biases in PNNL-MMF. The data sets of the PNNL-MMF and satellite observations are presented in the next section. Section 3 illustrates our definition of warm-rain clouds and some classifications (i.e., nonprecipitating, drizzle, and rain modes), and the analysis of observed and simulated warm-rain clouds are presented in section 4. Here the possible sources of model biases in PNNL-MMF such as microphysical parameterization, subgrid variability, or dynamical process are studied. Section 5 demonstrates the possible solutions to improve model performance in PNNL-MMF. The paper concludes in section 6 with a discussion and summary of key findings.

2. The Data

2.1. A-Train Satellite Observations

CloudSat flies as part of the A-Train constellation and carries a 94 GHz Cloud Profiling Radar (CPR) [*Stephens et al.*, 2008], which is sensitive to both cloud-and precipitation-sized particles. CloudSat has a horizontal resolution of 1.7 km along track by 1.4 km across track with a horizontal sampling interval of about 1.1 km and has a vertical resolution of 480 m. Since CloudSat is an active sensor to observe clouds, the CloudSat CPR can provide us with detailed vertical structures of clouds through radar reflectivity (Ze) profiles from the 2B-GEOPROF product [e.g., *Mace*, 2007; *Marchand et al.*, 2008]. The 2B-GEOPROF also includes a cloud mask to identify cloud. In this study, we use a cloud mask value $\geq$30, which is a high-confidence detection of clouds.

The Moderate Resolution Imaging Spectroradiometer (MODIS) instrument on Aqua, which is also a member of the A-Train satellite constellation, provides an estimate of cloud optical depth by measuring the amount of sunlight reflected from clouds. We use the MODIS collection 5.1 level 2 MYD06 cloud product of effective

particle radius (r_e), optical thickness (τ_c), and cloud top temperature [e.g., *Platnick et al.*, 2003]. The MODIS MYD06 cloud product is provided by MODIS retrievals collocated to the daytime CloudSat radar footprint. Cloud fraction and warm cloud fraction are estimated by both CloudSat CPR and MODIS MYD06.

For precipitation intensity, we use 2C-RAIN-PROFILE to estimate surface precipitation intensity along with the CloudSat CPR profiles. The 2C-RAIN-PROFILE product is developed by *Mitrescu et al.* [2010] and modified by *Lebsock and L'Ecuyer* [2011] to better represent warm-raindrop size distributions and evaporation. This rainfall product has been shown to agree with in situ estimates to within 20% of the mean precipitation observed in warm maritime clouds [*Rapp et al.*, 2013].

2.2. PNNL-MMF Model Simulation

PNNL-MMF is an extension of the Colorado State University (CSU) MMF [*Khairoutdinov et al.*, 2005, 2008] that has an embedded 2-D cloud-resolving model (CRM) in place of parameterizations in each grid column of a general circulation model (GCM). A detailed description of the PNNL-MMF is documented in *Wang et al.* [2011a, 2011b]. The host GCM (Community Atmosphere Model 5) has 30 vertical levels at a 1.9 × 2.5° horizontal grid. The embedded CRM includes 32 columns at 4 km horizontal grid spacing with 28 vertical layers. The time step for the host GCM is 10 min and that for the embedded CRM is 20 s. The PNNL-MMF uses a two-moment microphysics scheme from *Morrison et al.* [2005, 2009], which includes the autoconversion parameterization based on the KK scheme [*Khairoutdinov and Kogan*, 2000]. Rainwater mixing ratio is a prognostic model variable. The subgrid variability in cloud dynamics and cloud microphysics is explicitly resolved at spatial scales down to the resolution of the CRM. A 94 GHz Cloud Profiling Radar (CPR) instrument simulator is embedded in the PNNL-MMF. Following S15, output from PNNL-MMF is based on a 1 year simulation at 13:30 local time under seasonally varying climatological sea surface temperature.

3. Definitions of Warm-Rain Clouds

First we apply data filters to both the observations and model fields. For the CPR, we screen the data set based on 2B-GEOPROF cloud mask value ≥30. For PNNL-MMF we filter volumes where the sum of cloud water and rain mixing ratio ($q_c + q_r$) is less than 10^{-5} kg/kg. Then, to be selected, both observed and simulated warm-rain clouds must satisfy: (1) CPR > -28 dBZ [*Im et al.*, 2005] must be continuous from cloud top to cloud bottom, (2) cloud top temperature $\geq$ 273.15 K, and (3) cloud top pressure $\geq$ 500 hPa [*Chang and Li*, 2005]. This sampling criteria only selects single-layer warm clouds and avoids the case of ice cloud above warm clouds.

We also only use warm clouds over ocean to study cloud properties. Oceanic warm-rain clouds are further categorized by different modes by the column maximum radar reflectivity (Z_{max}): cloud (nonprecipitation) mode is $Z_{max} < -15$ dBZ, drizzle mode is -15 dBZ $< Z_{max} < 0$ dBZ, and rain mode is $Z_{max} > 0$ dBZ following our prior work [*Suzuki et al.*, 2011, 2015].

4. Comparisons Between Observed and Simulated Warm-Rain Clouds

Cloud fraction and cloud properties can be sensitive to resolutions. Since the resolutions between observations and the PNNL-MMF are quite different, it could cause some biases in the study. To conduct a fair comparison between the observation and the PNNL-MMF, we averaged three consecutive observation pixels together (~3.9 km) to come up with observations at the 4 km PNNL-MMF spatial scale.

4.1. Cloud Fraction and Optical Depth

Climate models are often evaluated by the observed cloud fraction and the basic observed cloud properties such as optical depth, cloud top height, and top-of-the-atmosphere flux [i.e., *Zhang et al.*, 2005; *Klein et al.*, 2013; *Konsta et al.*, 2015]. First, we compare the CPR cloud fraction between the A-Train observations (CloudSat and Aqua-MODIS) and PNNL-MMF. The spatial distribution (60°N–60°S) of total cloud fraction (%) and that of warm cloud fraction (%) based on the observations and PNNL-MMF are shown in Figure 1. The total cloud fraction is estimated as total number of cloudy-sky profiles divided by all profiles (cloudy-sky profiles + clear-sky profiles) within 10° × 10° grid box. The cloudy-sky profile is defined when a profile contains any CPR signals. The warm cloud fraction is estimated as total number of cloudy-sky profiles whose cloud top temperature (CTT) $>$ 273.15 K divided by all profiles (cloudy-sky profiles + clear-sky profiles)

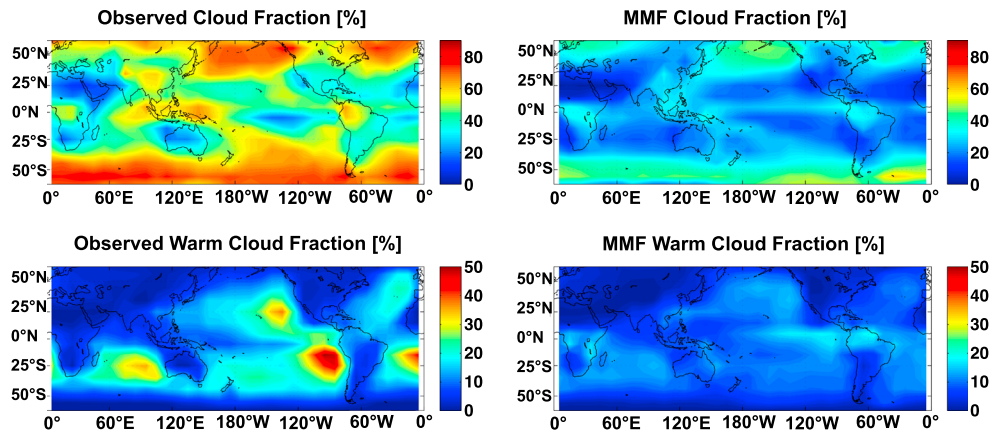

Figure 1. The spatial distribution (60°N–60°S) of (top) total cloud fraction and that of (bottom) warm cloud fraction based on the (left) observations and (right) PNNL-MMF. Unit is in %.

within 10° × 10° grid box. Spatial correlations between the observations and PNNL-MMF are high: 0.78 for the total cloud fraction and 0.81 for the warm cloud fraction. The PNNL-MMF captures the general patterns of cloud distributions fairly well. However, the amount of cloud coverage in PNNL-MMF is much lower than the observations. The lesser coverage of warm clouds in PNNL-MMF compared to the observations would act to lessen the net cooling effect of warm clouds. To maintain the top-of-the-atmosphere radiative fluxes comparable to the observations, simulated warm clouds must be thicker and/or warmer than observed clouds to enhance the net cooling effect. The presence of these compensating cloud errors is demonstrated next.

We will compare the observed and simulated total optical depth (τ) to test if simulated clouds are thicker than observed clouds. We also check how simulated τ varies among different modes (i.e., nonprecipitating mode, drizzle mode, and rain mode). Figure 2 represents the spatial distribution (60°N–60°S) of observed and simulated τ in the nonprecipitating mode ($Z_{\max} < -15$ dBZ), drizzle mode (-15 dBZ $< Z_{\max} < 0$ dBZ), and rain mode ($Z_{\max} > 0$ dBZ). Both observations and PNNL-MMF have smaller τ in the cloud mode and higher τ in the rain mode. PNNL-MMF captures the tendency of τ to increase as precipitation rate increases. However, PNNL-MMF has much higher τ than observations in all modes. The absolute amplitude differences between observations and PNNL-MMF are large, especially for the drizzle and rain modes. In terms of the fractional differences, the largest discrepancy between observations and PNNL-MMF can be found over the tropics, especially in the cloud and drizzle modes, where simulated tropical τ is more than 200% larger than observed tropical τ, demonstrating that the PNNL-MMF seems to have particular challenges in realistically representing shallow precipitating cumulus clouds. As we expected, simulated warm clouds are optically thicker to keep the top-of-the-atmosphere flux similar to the observations. Additionally, PNNL-MMF also does not produce realistic spatial patterns of τ. The spatial correlations between observations and PNNL-MMF are 0.10, 0.25, and 0.05 for the cloud, drizzle, and rain modes, respectively.

4.2. The Subgrid-Scale Variability

A unique aspect of the MMF is its explicit representation of the subgrid-scale variability of clouds and precipitation, which in principal permits a much more realistic representation of microphysical processes than conventional parameterization. Here we explore the subgrid variability, in the form of spatial homogeneity of τ (denoted as v_τ), in the observations and PNNL-MMF. Following *Lebsock et al.* [2013], v_τ is defined as $v_\tau = \left(\frac{\overline{\tau}}{\sigma_\tau}\right)^2$, where $\overline{\tau}$ is the spatial mean of τ and σ_τ is the spatial standard deviation of τ. A larger value of v_τ means more spatially homogeneous clouds. In the observations v_τ is calculated along a 110 km CloudSat ground track, whereas in the MMF it is calculated from the 124 km 2-D embedded CRM. Figure 3 shows the spatial distribution of observed and simulated v_τ in the cloud, drizzle, and rain modes. Both the observations and PNNL-MMF have higher v_τ in the cloud mode and lower v_τ in the rain mode. Unlike the mean τ, the

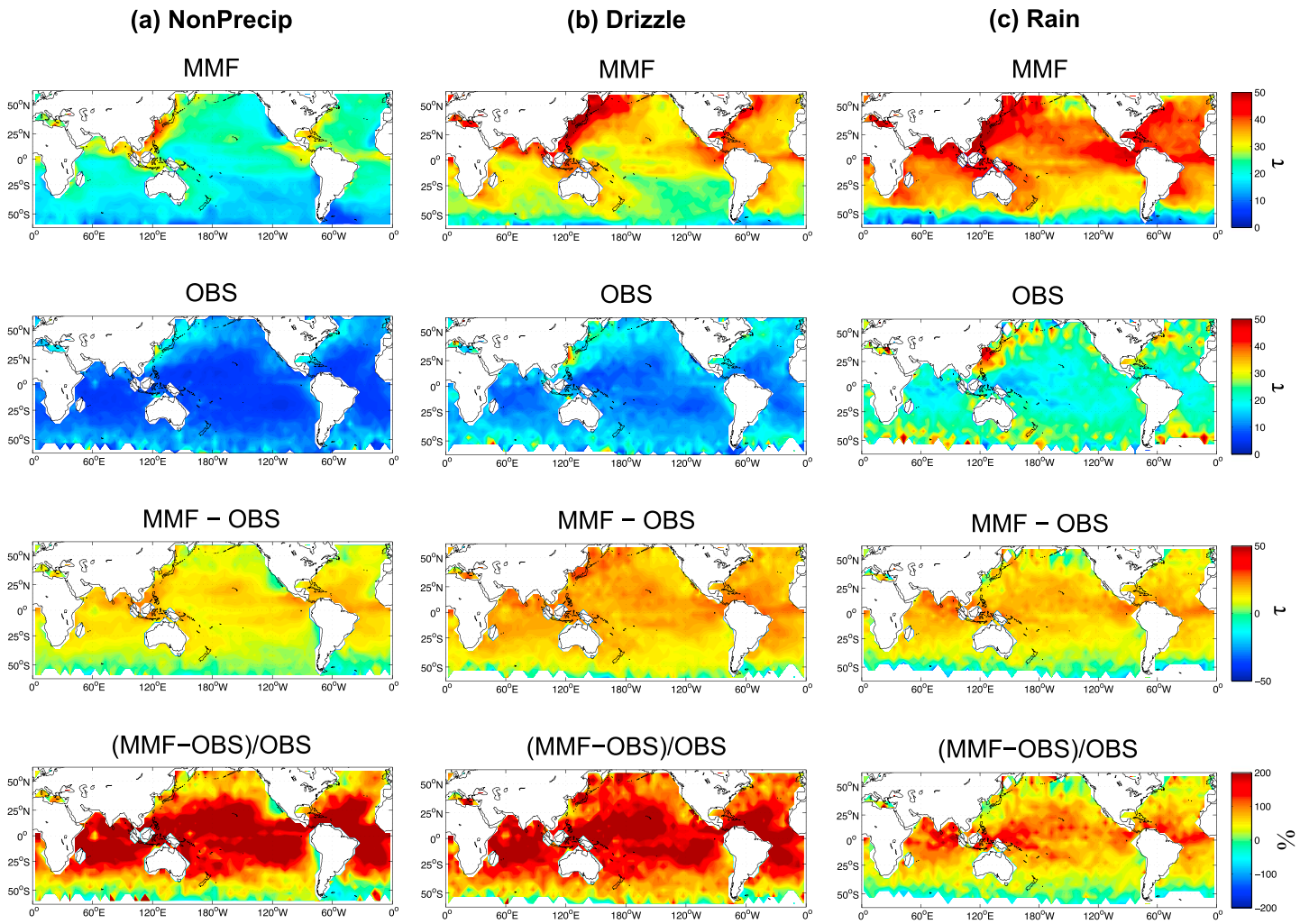

Figure 2. The spatial distribution (60°N–60°S) of observed and simulated optical depth (τ) in the (a) nonprecipitating mode (left, $Z_{max} < -15$dBZ), (b) drizzle mode (middle, -15 dBZ $< Z_{max} < 0$ dBZ), and (c) rain mode (right, $Z_{max} > 0$ dBZ) based on (first row) PNNL-MMF, (second row) the observation, (third row) the absolute difference between PNNL-MMF and the observations, and (fourth row) the fractional difference between PNNL-MMF and the observations.

amplitude of ν_τ agrees well between observations and the PNNL-MMF, except around 50°N/S. The spatial correlations between observations and PNNL-MMF are 0.53, 0.47, and 0.22 for the cloud, drizzle, and rain modes, respectively. The spatial patterns of ν_τ agree fairly well between the observations and PNNL-MMF in the cloud mode and drizzle mode, but not in the rain mode, although this may partly be explained by a small number of samples in the observations. Overall, the subgrid-scale variability is well represented in the PNNL-MMF model. This result suggests that the possible sources of model biases are likely due to errors in its microphysics or dynamics rather than errors in the subgrid-scale representation of cloudiness.

4.3. Cloud Properties and Microphysics

Figure 4 compares the histograms of cloud top height (CTH), cloud top pressure (CTP), cloud top temperature (CTT), and Z_{max} between the A-Train observations and PNNL-MMF. Observed cloud tops are frequently found around 1.4 km or 850 hPa, while simulated cloud tops are likely to be found around 1 and 1.6 km or 900 hPa. Simulated warm clouds also have warmer cloud top temperature than observed warm clouds, which would result in enhanced radiative cooling to space by the simulated clouds and helping compensate for the less cloud fraction to maintain the correct radiative balance.

The most intriguing feature in Figure 4 lies in the difference in the Z_{max} histograms between the observations and PNNL-MMF: while the observations show the bell-shaped distribution with high occurrence between

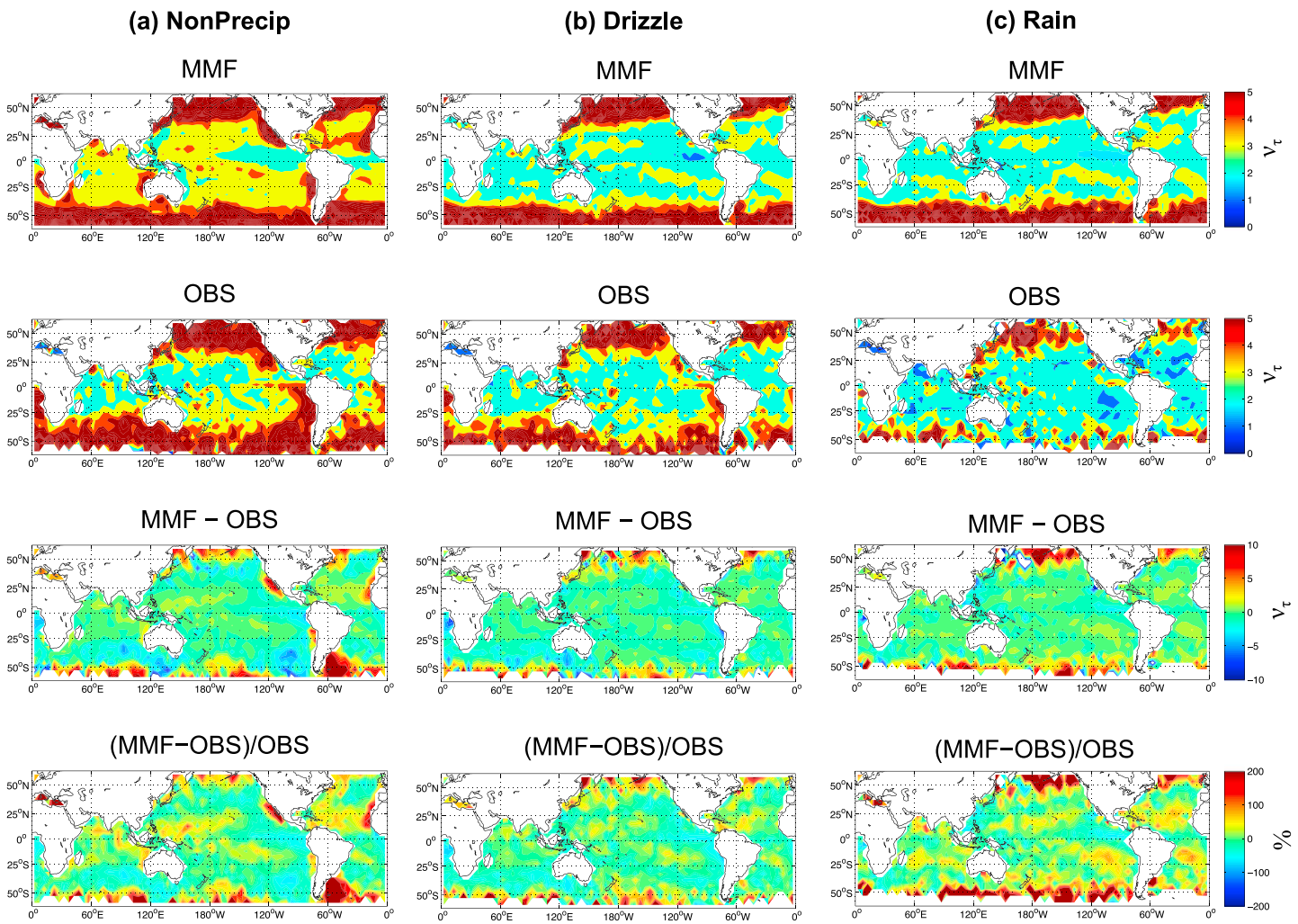

Figure 3. The spatial distribution (60°N–60°S) of observed and simulated subgrid variability, homogeneity of τ (ν_τ), in the (a) nonprecipitating mode (left, $Z_{\max} < -15$ dBZ), (b) drizzle mode (middle, -15 dBZ $< Z_{\max} < 0$ dBZ), and (c) rain mode (right, $Z_{\max} > 0$ dBZ) based on (first row)PNNL-MMF, (second row) the observation, (third row) the absolute difference between PNNL-MMF and the observations, and (fourth row) the fractional difference between PNNL-MMF and the observations.

-20 to -10 dBZ (nonprecipitation to light drizzle mode), PNNL-MMF shows a bimodal distribution with two peaks over nonprecipitating mode ($Z_{\max} < -15$ dBZ) and rain mode ($Z_{\max} > 0$ dBZ). It is also interesting to point out that simulated warm clouds have $Z_{\max} > 15$ dBZ, which indicates either very large precipitation water contents and/or drop sizes. Reflectivities this large are rarely observed in CloudSat observations.

Unlike other models, which tend to produce precipitation that is too frequent and too light, PNNL-MMF does not favor producing drizzle mode clouds. Instead, when PNNL-MMF produces precipitation it tends to be heavier than the observations. To better understand this behavior, we now examine the cloud water path. We calculate simulated and observed liquid water path (LWP $= \frac{2}{3}\rho_\omega r_e \tau$, where ρ_ω is liquid water density), along with a bulk liquid water content $\left(\text{LWC} = \frac{\text{LWP}}{\text{CTH}}\right)$. These variables together with CTH and cloud top effective particle radius (r_e) in the cloud, drizzle, and rain modes are summarized in Figure 5. Both simulated and observed CTH and LWP increase from the nonprecipitating modes to rain modes. Observed LWC and r_e also increases from the nonprecipitating modes to rain modes, while simulated LWC and r_e in rain modes is comparable to, if not slightly lower than, those in nonprecipitating or drizzle modes. Simulated r_e is smaller than observed r_e in all stages. However, r_e from the MODIS observation is known to have high biases. For example, compared to an in situ r_e, MODIS r_e is 1 to 2 μm higher for stratocumulus clouds off the coast of Chile and Peru [*Painemal and Zuidema*, 2011] and 7 to 12 μm higher for trade wind clouds for the tropical

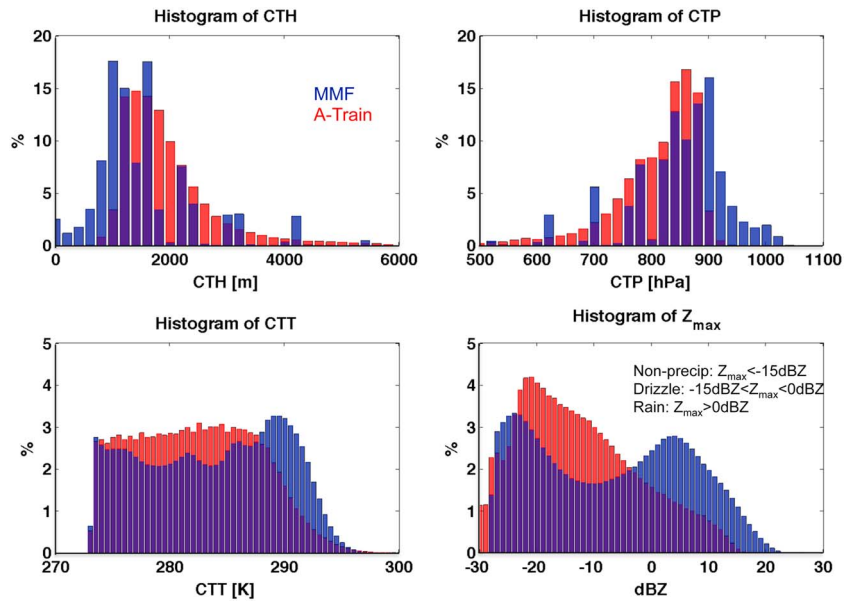

Figure 4. The histograms of cloud top height (CTH), cloud top pressure (CTP), cloud top temperature (CTT), and Z_{max} between the A-Train observations (red) and PNNL-MMF (blue).

western Atlantic [*Haney*, 2013]. Therefore, it is hard to interpret amplitude bias of r_e between the observation and PNNL-MMF. Overall, PNNL-MMF overestimates LWP and LWC in all modes. In particular, the LWC is very large relative to the observations. This is not surprising since the rain formation in PNNL-MMF is known to be less efficient than observations (S15). Because the simulated LWP is able to become too large before the onset of precipitation, it is possible that once precipitation initiates, the simulated warm clouds have a potential to produce heavier rain than reality through an extremely efficient accretion process. To test this possibility, the intensity of precipitation between the observations and PNNL-MMF is compared next (Figure 6).

In the cloud mode ($Z_{max} < -15$ dBZ), virtually no precipitation reaches the surface as the droplets evaporate in the air. Although PNNL-MMF has P = 0[mm/h] in the mean state for the cloud mode (Figure 6, left), PNNL-MMF has large nonzero outliers (Figure 6, right). Light drizzle is also expected to evaporate, and thus,

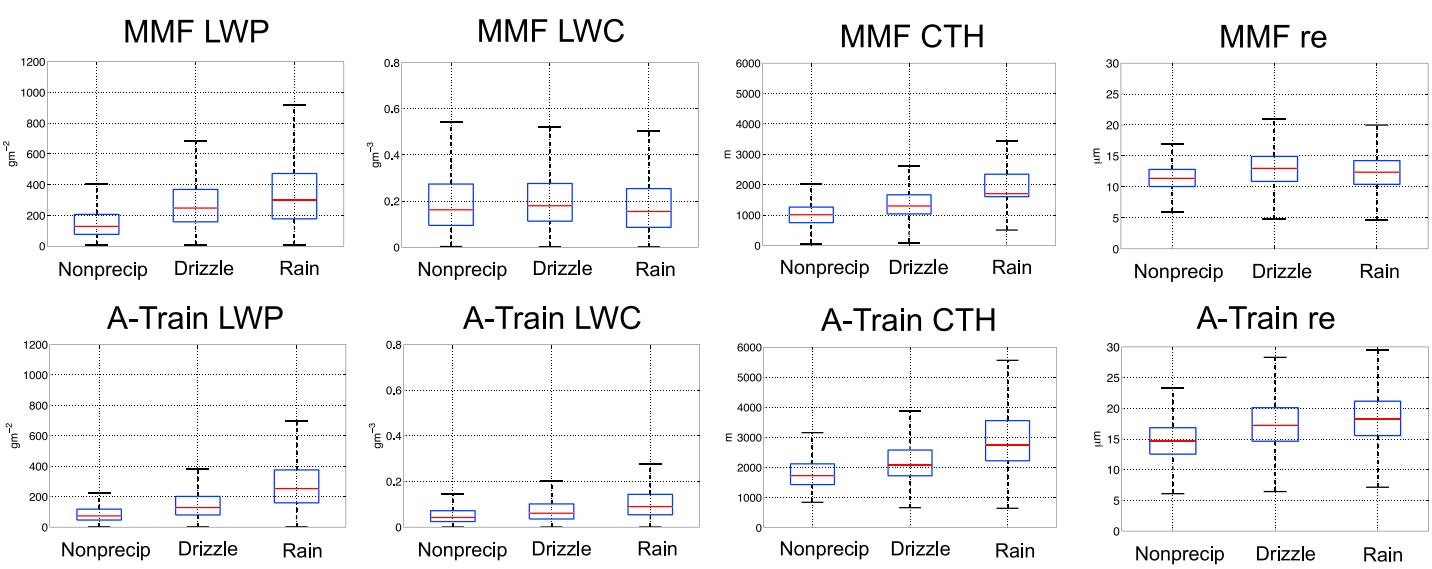

Figure 5. The box-and-whisker plots of (top) simulated and (bottom) observed liquid water path (LWP), liquid water content $\left(\mathrm{LWC} = \frac{\mathrm{LWP}}{\mathrm{CTH}}\right)$, together with CTH and cloud top effective radius (r_e) in the cloud, drizzle, and rain modes.

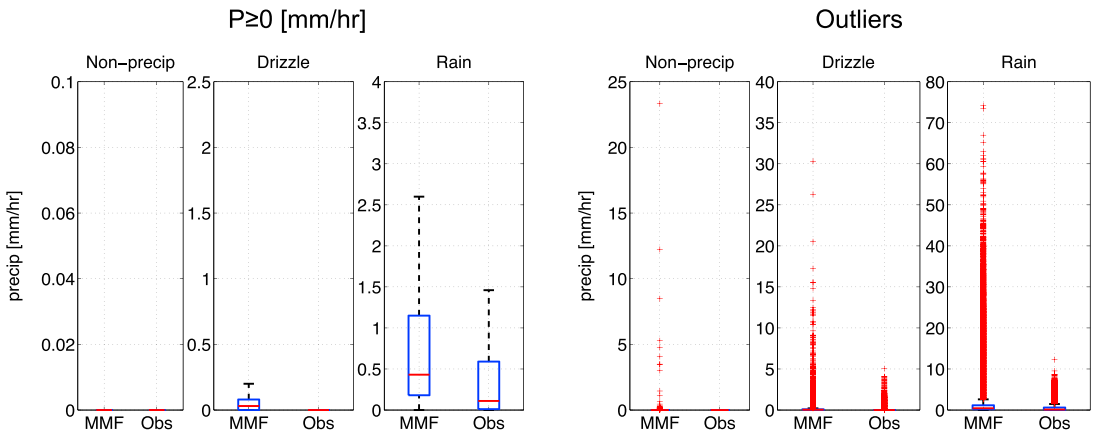

Figure 6. The intensity of precipitation between the observations and PNNL-MMF using box-and-whisker plots. (top left) The intensity of precipitation including nonprecipitating cases (precipitation (*P*) is equal to 0 (mm/h)). (top right) The outliers.

the observed drizzle mode shows $P = 0$[mm/h] in the mean state. Although the simulated drizzle mode has similar mean precipitation value compared to the observations, the outliers in PNNL-MMF are again larger than the observations. We speculate that PNNL-MMF might have drops that are too large to evaporate before hitting the ground, and thus, PNNL-MMF has large outliers in cloud and drizzle modes. For the rain mode, although observed and simulated rain intensities are comparable in the mean state, the range of intensity including outliers is very different between the observations (0 to 13.09 mm/h) and PNNL-MMF (0 to 82.00 mm/h). These results indicate that the PNNL-MMF produces about the correct mean rain rate to satisfy atmospheric energy balance with an incorrect distribution of rates. There are compensating errors in PNNL-MMF between precipitation frequency and intensity in warm clouds, a feature which is qualitatively similar, but opposite in sign, to those found in other global models [*Stephens et al.*, 2010].

Correlations between variables can provide more insight into the model microphysics than comparison of single variables. In particular, Figure 7 illustrates the intensity of precipitation as a function of LWP, which provides a measure of the efficiency of the precipitation process. Rain rates increase with increasing LWP in both the model and the observations. It is interesting to point out that the tendency of mean precipitation intensity over LWP is very similar between the model and the observations; however, the median precipitation intensity is less sensitive to LWP in PNNL-MMF compared to the observations. As S15 suggested, it is clear that the rain efficiency is lower in PNNL-MMF than the observations in terms of the median; however, it is also true that LWP is generally much higher in PNNL-MMF than the observations (Figure 5). There is therefore a compensating error between the PNNL-MMF cloud water content and the low efficiency of precipitation in PNNL-MMF, which results in approximately the correct mean rainfall rate.

5. Constraint on Microphysical Parameterization

The PNNL-MMF model has low precipitation efficiency, and a question here to be addressed is what controls the precipitation efficiency. As described in section 1, the precipitation process in models is represented as the combination of autoconversion and accretion processes. The autoconversion process directly converts cloud water to rainwater, while the accretion process collects cloud water by falling rain. S15 demonstrated that the different autoconversion schemes produced different behaviors of precipitation processes, and the precipitation formation was mainly triggered by the autoconversion process. In general, the parameterization of the autoconversion rate can be described as

$$\left(\frac{\partial q_r}{\partial t}\right)_{\text{aut}} = C \cdot \frac{q_c^{\alpha}}{N_c^{\beta}},$$

where N_c is cloud droplet number concentration (cm^{-3}) and q_c and q_r are cloud and rainwater mixing ratios (kg kg^{-1}), respectively. S15 showed that different values of α and β, especially β, controlled the dependency on number concentration of cloud, drizzle, and rain modes, and the models based on the KK scheme simulated the most realistic distribution of cloud, drizzle, and rain modes. In the KK scheme, $\alpha = 2.47$ and $\beta = 1.79$,

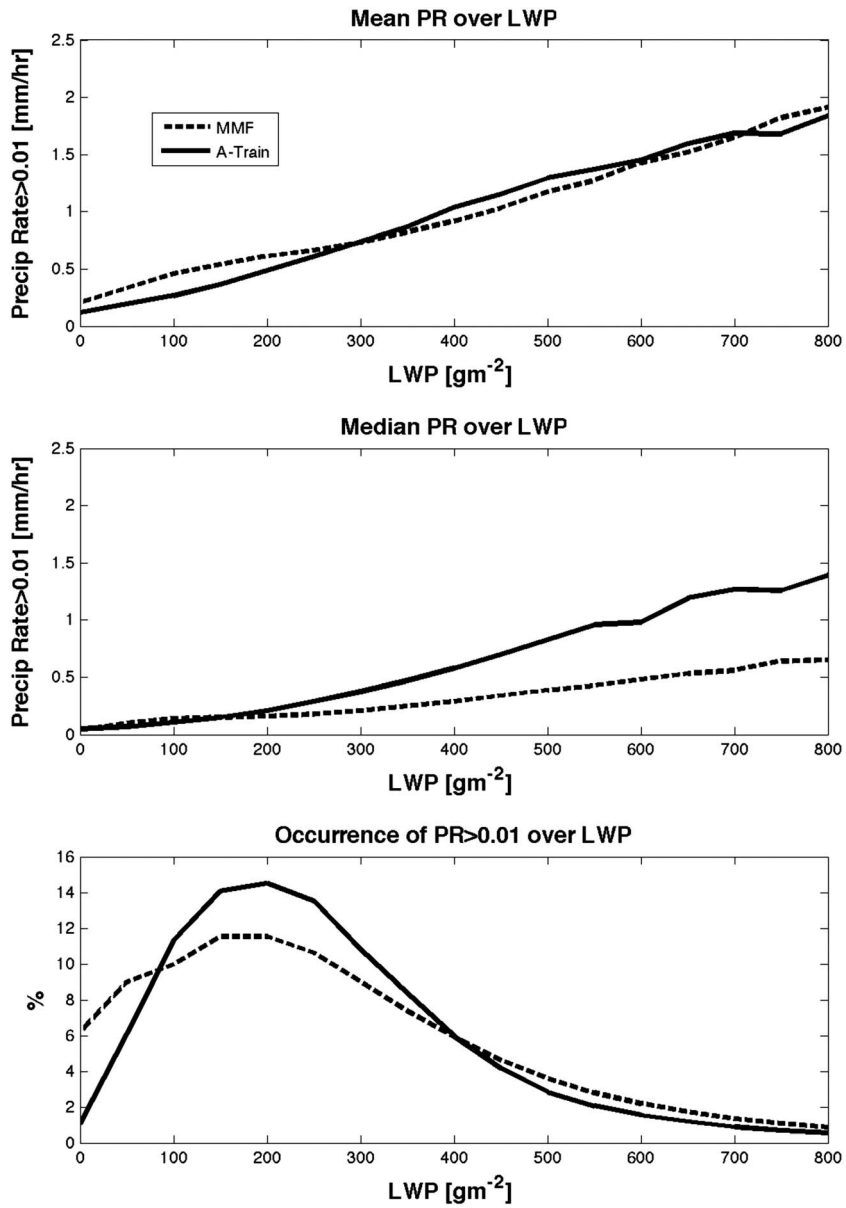

Figure 7. The (first row) mean and (second row) median precipitation intensities as a function of LWP, together with the occurrence frequency (%) of LWP (third row) based on the observations (black solid lines) and PNNL-MMF (black dotted lines).

and a tunable parameter *C* is set to be 1350. As described in section 2.2, PNNL-MMF uses the autoconversion parameterization based on the KK scheme. Although the KK scheme simulated the most realistic warm-rain formation process as documented in S15, the fact of lower precipitation efficiency in PNNL-MMF suggests that the current autoconversion rate used in PNNL-MMF needs some tuning. In this section, we investigate how the precipitation efficiency can be improved by changing the tunable parameter *C*.

5.1. A One-Dimensional Model

The one-dimensional model used in this study is introduced in *Suzuki et al.* [2013, 2015]. The liquid precipitation process in the model is characterized by two mixing ratios of cloud water and rainwater. These two mixing ratios are allowed to have vertical profiles and to develop with time in the model. The process of microphysical precipitation is assumed to occur with a water conversion rate that is due to a combination of autoconversion and accretion processes.

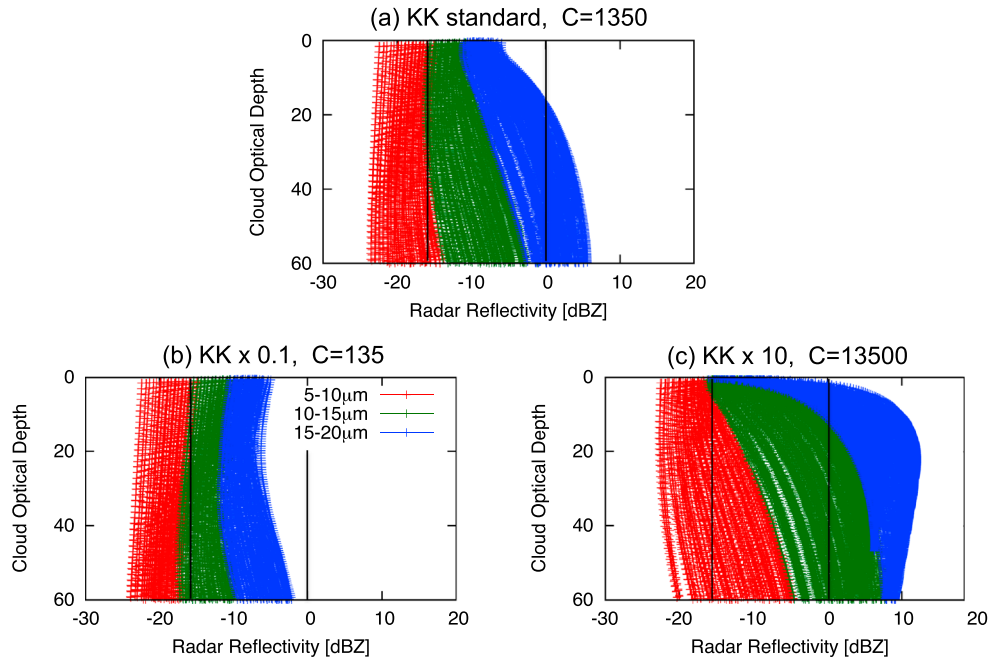

Figure 8. Simulated vertical profiles of radar reflectivity as a function of cloud optical depth based on three different values of (a) C = 1350, (b) C = 135, and (c) C = 13500. The red, green, and blue profiles are the radar reflectivity profiles for r_e = 5–10 μm, 10–15 μm, and 15–20 μm, respectively.

The QuickBeam radar signal simulator of *Haynes et al.* [2007] is also applied in a form that is adjusted to the spectral-bin microphysics scheme in order to simulate radar reflectivity profiles in the one-dimensional model. The model is numerically integrated with an initial condition of zero for the mixing ratios of both cloud and liquid particles for the entire cloud layer until the steady state is achieved under assumptions of different values of cloud droplet number concentrations and geometrical cloud thickness. This produces different values of the cloud top effective radius that are used to classify the radar reflectivity profiles obtained from the model. The model performed with varying thermodynamic conditions within a reasonable range. A more detailed description of the model framework including the governing equation is documented in *Suzuki et al.*, 2013, 2015, and *Takahashi et al.*, 2017.

5.2. Interpretation Using a One-Dimensional Model

We use the one-dimensional model to explore how the precipitation efficiency in PNNL-MMF differs by changing the tunable parameter C. In order to test this, simulated vertical profiles of radar reflectivity as a function of cloud optical depth are provided based on three different values of C (i.e., the original value,10 times smaller than the original value, and10 times bigger than the original value), and the results are summarized in Figure 8. The vertical black bars in Figure 8 at −15 and 0 dBZ show the imposed delineation between the cloud/drizzle/rain categorizations. The radar reflectivity profiles vary with different cloud top effective radius (r_e). For example, when C = 1350 (Figure 8a, the original case), the profiles for r_e = 5–10 μm (red profiles) are in the category of cloud (nonprecipitation) mode since their radar reflectivity is less than −15 dBZ around the cloud base (cloud optical depth ~ 60). The profiles for r_e = 10–15 μm (green profiles) produce drizzle (−15 dBZ to 0 dBZ), and majority of profiles for r_e = 15–20 μm (blue profiles) produce rain (greater than 0 dBZ) around cloud base. Now we demonstrate how the distributions of cloud, drizzle, and rain modes are controlled by the value of C. When C = 135 (10 times smaller than the original case; Figure 8b), it is clear that the range of precipitation decreases. The profiles shift toward left-hand side (i.e., toward smaller radar reflectivity) and the distributions of cloud, drizzle, and rain modes become narrower than the original case (Figure 8a). Half of the profiles belongs to cloud mode and the other half belongs to drizzle mode, and none of the profiles produce rain mode. On the other hand, when C = 13500 (10 times bigger than the original case; Figure 8c), the range of precipitation increases. The profiles shift toward the right-hand side (i.e., toward the larger radar reflectivity), and the distributions of cloud and drizzle modes become wider compared to the

original case (Figure 8a). Even some of profiles for r_e = 5–10 μm can produce drizzle. The reason why we do not see a wider range in rain mode around the cloud base is because the radar reflectivity enters the Mie Scattering regime and further attenuates with depth when the precipitation is intense effectively limiting the maximum physically possible reflectivity near 20 dBZ.

As demonstrated in Figure 8, the precipitation efficiency is sensitive to *C* and it increases with increasing *C*. It is very interesting to test how the overall model performance in PNNL-MMF will improve by using larger *C* values. Our hypothesis is that the compensating errors in PNNL-MMF will be reduced by using larger *C* values, and we will test this in the near future.

Furthermore, it appears that there is a tendency for PNNL-MMF to produce heavier precipitation than the observations, possibly because the coalescence process becomes overly efficient as the cloud water content reaches unrealistically high values. This can be because currently PNNL-MMF has the Marshall-Palmer distribution [*Marshall and Palmer*, 1948], which can produce an exponential drop-size distribution. Here we suggest using a different distribution [*Abel and Boutle*, 2012] used by the Met Office, which better represents the full spectrum of precipitation rates and was shown to improve the representation of light precipitation processes in that model. This also will be studied in the future.

6. Summary

This study documents key model biases in the PNNL-MMF of warm cloud microphysics. To identify the major sources of model biases in PNNL-MMF, microphysical and subgrid variability statistics in PNNL-MMF are compared to those from the A-Train observations. The key findings are as follows:

1. PNNL-MMF generally favors clear-sky rather than cloudy-sky. To compensate for the smaller net cooling effect due to smaller warm cloud coverage, warm clouds in PNNL-MMF are found to be optically thicker and warmer than the observations.
2. Subgrid-scale variability of optical depth is realistically simulated, which suggests that the biases observed in simulated clouds result from a combination of microphysical and dynamical errors, rather than subgrid-scale representation errors.
3. Error compensation between the larger cloud water content and the lower efficiency of precipitation in PNNL-MMF is found, which leads the model to have approximately the correct mean rainfall rate with an incorrect distribution of rates.
4. It appears that there is a tendency for the PNNL-MMF to produce heavier precipitation (when it occurs) than the observations possibly because the coalescence process becomes overly efficient as the cloud water content reaches unrealistically high values.
5. The precipitation efficiency is sensitive to *C*, a tunable parameter in the parameterization of the autoconversion rate. Using larger *C* values might improve overall model performance and reduce the compensating errors in PNNL-MMF.

As demonstrated in S15 and this study, the autoconversion rate plays a key role in controlling the precipitation efficiency as well as the distribution of cloud, drizzle, and rain modes. Since PNNL-MMF has low precipitation efficiency, our results suggest using larger *C* values to increase the precipitation efficiency. In a similar manner, using smaller *C* values might help improving overall model performances for those GCMs with high precipitation efficiency. We would like to verify this in the near future as well.

Acknowledgments
The research was carried out at the Jet Propulsion Laboratory, California Institute of Technology, under a contract with the National Aeronautics and Space Administration (NASA). The study was supported by grant NNN13D455T. K. Suzuki was supported by NOAA's Climate Program Office's Modeling, Analysis, Predictions, and Projections program with the grant NA15OAR4310153, JAXA/EarthCARE and JAXA/GCOM-C projects. The data of A-Train observations can be found from the CloudSat Data Processing Center at www.cloudsat.cira.colostate.edu. We are also grateful to two anonymous reviewers for their valuable comments.

References

Abel, S. J., and I. A. Boutle (2012), An improved representation of the raindrop size distribution for single-moment microphysics schemes, *Q. J. R. Meteorol. Soc.*, *138*(669), 2151–2162.

Albrecht, B. A. (1989), Aerosols, cloud microphysics, and fractional cloudiness, *Science*, *245*, 1227–1230.

Albrecht, B. A. (1993), Effects of precipitation on the thermodynamic structure of the trade wind boundary layer, *J. Geophys. Res.*, *98*, 7327–7337.

Chang, F. L., and Z. Li (2005), A near-global climatology of single-layer and overlapped clouds and their optical properties retrieved from Terra/MODIS data using a new algorithm, *J. Clim.*, *18*(22), 4752–4771.

Déqué, M., D. P. Rowell, D. Lüthi, F. Giorgi, J. H. Christensen, B. Rockel, D. Jacob, E. Kjellström, M. de Castro, and B. J. J. M. van den Hurk (2007), An intercomparison of regional climate simulations for Europe: Assessing uncertainties in model projections, *Clim. Change*, *81*(1), 53–70.

Ellingson, R. G., J. Ellis, and S. Fels (1991), The intercomparison of radiation codes used in climate models: Long wave results, *J. Geophys. Res.*, *96*, 8929–8953.

Golaz, J. C., L. W. Horowitz, and H. Levy (2013), Cloud tuning in a coupled climate model: Impact on 20th century warming, *Geophys. Res. Lett.*, *40*, 2246–2251, doi:10.1002/grl.50232.

Haney, C. O. (2013), Cloud drop effective radius for trade wind cumuli observed during RICO by aircraft and MODIS, MS thesis, Univ. of Ill. at Urbana-Champaign, 89 pp.

Haynes, J. M., R. Marchand, Z. Luo, A. Bodas-Salcedo, and G. L. Stephens (2007), A multi-purpose radar simulation package: QuickBeam, *Bull. Am. Meteorol. Soc.*, *88*, 1723–1727.

Henderson-Sellers, A., Z. L. Yang, and R. E. Dickinson (1993), The project for intercomparison of land-surface parameterization schemes, *Bull. Am. Meteorol. Soc.*, *74*(7), 1335–1349.

Huang, D., and Y. Liu (2014), Statistical characteristics of cloud variability. Part 2: Implication for parameterizations of microphysical and radiative transfer processes in climate models, *J. Geophys. Res. Atmos.*, *119*, 10,829–10,843, doi:10.1002/2014JD022003.

Im, E., C. Wu, and S. L. Durden (2005), Cloud profiling radar for the CloudSat mission, *IEEE Trans. Aerosp. Electron. Syst.*, *20*, 15–18, doi:10.1109/MAES.2005.1581095.

Khairoutdinov, M., and Y. Kogan (2000), A new cloud physics parameterization in a large-eddy simulation model of marine stratocumulus, *Mon. Weather Rev.*, *128*(1), 229–243.

Khairoutdinov, M., D. Randall, and C. DeMott (2005), Simulations of the atmospheric general circulation using a cloud-resolving model as a superparameterization of physical processes, *J. Atmos. Sci.*, *62*(7), 2136–2154.

Khairoutdinov, M., C. DeMott, and D. Randall (2008), Evaluation of the simulated interannual and subseasonal variability in an AMIP-style simulation using the CSU multiscale modeling framework, *J. Clim.*, *21*(3), 413–431.

Klein, S. A., Y. Zhang, M. D. Zelinka, R. Pincus, J. Boyle, and P. J. Gleckler (2013), Are climate model simulations of clouds improving? An evaluation using the ISCCP simulator, *J. Geophys. Res. Atmos.*, *118*, 1329–1342, doi:10.1002/jgrd.50141.

Konsta, D., J. L. Dufresne, H. Chepfer, A. Idelkadi, and G. Cesana (2015), Use of A-train satellite observations (CALIPSO–PARASOL) to evaluate tropical cloud properties in the LMDZ5 GCM, *Clim. Dyn.*, 1–22.

Lebsock, M. D., and T. S. L'Ecuyer (2011), The retrieval of warm rain from CloudSat, *J. Geophys. Res.*, *116*, D20209, doi:10.1029/2011JD016076.

Lebsock, M., H. Morrison, and A. Gettelman (2013), Microphysical implications of cloud-precipitation covariance derived from satellite remote sensing, *J. Geophys. Res. Atmos.*, *118*, 6521–6533, doi:10.1002/jgrd.50347.

Mace, G. (2007), Level 2 GEOPROF product process description and interface control document algorithm version 5.3, NASA Jet Propulsion Lab.

Marchand, R., G. G. Mace, T. Ackerman, and G. Stephens (2008), Hydrometeor detection using CloudSat—An Earth-orbiting 94-GHz cloud radar, *J. Atmos. Oceanic Technol.*, *25*(4), 519–533.

Marshall, J. S., and W. M. K. Palmer (1948), The distribution of raindrops with size, *J. Meteorol.*, *5*(4), 165–166.

Miller, M. A., M. P. Jensen, and E. E. Clothiaux (1998), Diurnal cloud and thermodynamic variations in the stratocumulus transition regime: A case study using in situ and remote sensors, *J. Atmos. Sci.*, *55*(13), 2294–2310.

Mitrescu, C., T. L'Ecuyer, J. Haynes, S. Miller, and J. Turk (2010), CloudSat precipitation profiling algorithm-model description, *J. Appl. Meteorol. Climatol.*, *49*(5), 991–1003.

Morrison, H., J. A. Curry, and V. I. Khvorostyanov (2005), A new double-moment microphysics parameterization for application in cloud and climate models. Part I: Description, *J. Atmos. Sci.*, *62*(6), 1665–1677.

Morrison, H., G. Thompson, and V. Tatarskii (2009), Impact of cloud microphysics on the development of trailing stratiform precipitation in a simulated squall line: Comparison of one-and two-moment schemes, *Mon. Weather Rev.*, *137*(3), 991–1007.

Painemal, D., and P. Zuidema (2011), Assessment of MODIS cloud effective radius and optical thickness retrievals over the Southeast Pacific with VOCALS-REx in situ measurements, *J. Geophys. Res.*, *116*, D24206, doi:10.1029/2011JD016155.

Pedersen, C. A., and J. G. Winther (2005), Intercomparison and validation of snow albedo parameterization schemes in climate models, *Clim. Dyn.*, *25*(4), 351–362.

Pincus, R., and S. A. Klein (2000), Unresolved spatial variability and microphysical process rates in large-scale models, *J. Geophys. Res.*, *105*, 27,059–27,065, doi:10.1029/2000JD900504.

Platnick, S., M. D. King, S. A. Ackerman, W. P. Menzel, B. A. Baum, J. C. Riedi, and R. A. Frey (2003), The MODIS cloud products: Algorithms and examples from Terra, *IEEE Trans. Geosci. Remote Sens.*, *41*, 459–473.

Prein, A. F., et al. (2015), A review on regional convection-permitting climate modeling: Demonstrations, prospects, and challenges, *Rev. Geophys.*, *53*, 323–361, doi:10.1002/2014RG000475.

Rapp, A. D., M. D. Lebsock, and T. S. L'Ecuyer (2013), Low cloud precipitationclimatology in the southeastern Pacific marine stratocumulus region using CloudSat, *Environ. Res. Lett.*, *8*, 014027, doi:10.1088/1748-9326/8/1/014027.

Raut, E. K., and V. E. Larson (2016), A flexible importance sampling method for integrating subgrid processes, *Geosci. Model Dev.*, *9*(1), 413–429.

Stephens, G. L., et al. (2002), The CloudSat mission and the A-Train: A new dimension of space-based observations of clouds and precipitation, *Bull. Am. Meteorol. Soc.*, *83*(12), 1771–1790.

Stephens, G. L., et al. (2008), CloudSat mission: Performance and early science after the first year of operation, *J. Geophys. Res.*, *113*, D00A18, doi:10.1029/2008JD009982.

Stephens, G. L., T. L'Ecuyer, R. Forbes, A. Gettlemen, J. C. Golaz, A. Bodas-Salcedo, K. Suzuki, P. Gabriel, and J. Haynes (2010), Dreary state of precipitation in global models, *J. Geophys. Res.*, *115*, D24211, doi:10.1029/2010JD014532.

Suzuki, K., G. L. Stephens, S. C. Van Den Heever, and T. Y. Nakajima (2011), Diagnosis of the warm rain process in cloud-resolving models using joint CloudSat and MODIS observations, *J. Atmos. Sci.*, *68*(11), 2655–2670.

Suzuki, K., J. C. Golaz, and G. L. Stephens (2013), Evaluating cloud tuning in a climate model with satellite observations, *Geophys. Res. Lett.*, *40*, 4464–4468, doi:10.1002/grl.50874.

Suzuki, K., G. Stephens, A. Bodas-Salcedo, M. Wang, J. C. Golaz, T. Yokohata, and T. Koshiro (2015), Evaluation of the warm rain formation process in global models with satellite observations, *J. Atmos. Sci.*, *72*(10), 3996–4014.

Takahashi, H., K. Suzuki, and G. Stephens (2017), Land–ocean differences in the warm-rain formation process in satellite and ground-based observations and model simulations, *Q. J. R. Meteorol. Soc.*, *143*(705), 1804–1815, doi:10.1002/qj.3042.

Wang, M., et al. (2011a), The multi-scale aerosol-climate model PNNL-MMF: Model description and evaluation, *Geosci. Model Dev.*, *4*(1), 137–168, doi:10.5194/Gmd-4-137-2011.

Wang, M., S. Ghan, M. Ovchinnikov, X. Liu, R. Easter, E. Kassianov, Y. Qian, and H. Morrison (2011b), Aerosol indirect effects in a multi-scale aerosol-climate model PNNL-MMF, *Atmos. Chem. Phys.*, *11*(11), 5431.

Wood, R. (2000), Parametrization of the effect of drizzle upon the droplet effective radius in stratocumulus clouds, *Q. J. R. Meteorol. Soc.*, *126*(570), 3309–3324.

Zhang, M. H., et al. (2005), Comparing clouds and their seasonal variations in 10 atmospheric general circulation models with satellite measurements, *J. Geophys. Res.*, *110*, D15S02, doi:10.1029/2004JD005021.